

# How Malaria Parasites Reduce the Deformability of Infected Red Blood Cells

S. Majid Hosseini<sup>†</sup> and James J. Feng<sup>†\*</sup>

<sup>†</sup>Department of Chemical and Biological Engineering and <sup>‡</sup>Department of Mathematics, University of British Columbia, Vancouver, British Columbia, Canada

**ABSTRACT** The pathogenesis of malaria is largely due to stiffening of the infected red blood cells (RBCs). Contemporary understanding ascribes the loss of RBC deformability to a 10-fold increase in membrane stiffness caused by extra cross-linking in the spectrin network. Local measurements by micropipette aspiration, however, have reported only an increase of ~3-fold in the shear modulus. We believe the discrepancy stems from the rigid parasite particles inside infected cells, and have carried out numerical simulations to demonstrate this mechanism. The cell membrane is represented by a set of discrete particles connected by linearly elastic springs. The cytosol is modeled as a homogeneous Newtonian fluid, and discretized by particles as in standard smoothed particle hydrodynamics. The malaria parasite is modeled as an aggregate of particles constrained to rigid-body motion. We simulate RBC stretching tests by optical tweezers in three dimensions. The results demonstrate that the presence of a sizeable parasite greatly reduces the ability of RBCs to deform under stretching. With the solid inclusion, the observed loss of deformability can be predicted quantitatively using the local membrane elasticity measured by micropipettes.

## INTRODUCTION

Malaria is caused by mosquito-borne parasites of the genus *Plasmodium*, of which *Plasmodium falciparum* is a commonly studied species. The infective cycle consists of the ring, trophozoite, and schizont stages, with progressive changes in the shape, size, and structure of the infected red blood cell (iRBC) as well as those of the parasite itself. Mechanically, the iRBC gradually loses its deformability and becomes more easily adhered to the vascular walls and to other cells. When stretched by optical tweezers, the overall deformation of the iRBC decreases by several folds (1). The prevailing thinking in the literature is that the higher rigidity of the iRBC is due to remodeling of the RBC cytoskeleton by parasite-derived proteins. Recent numerical simulations of cell stretching have expressed this rigidification in terms of an elevated shear modulus  $G_s$  for the cell membrane. In the late stages of infection,  $G_s$  is estimated to be as high as 60  $\mu\text{N/m}$  (1–3), up from roughly 6  $\mu\text{N/m}$  for healthy RBCs (4–6). However, when the membrane is probed locally by micropipette aspiration, a much smaller increase in the membrane modulus is recorded, with  $G_s$  at about 15  $\mu\text{N/m}$  (5,6). This is too low to account for the reduced deformation of the whole cell measured by stretching.

Aside from  $G_s$ , whole-cell deformability also depends on the shape of the cell (its surface-area/volume ratio), the cytoplasmic viscosity, and the presence of the solid parasite inside (5,7). In particular, Nash et al. (5) speculated that “the main factor in the drastic loss of deformability of the trophozoites and schizonts was the presence of the large, very resistant parasite itself.” If proven, this would explain

the discrepancy between the relatively modest increase in membrane rigidity and the marked loss of whole-cell deformability. Experimentally, however, it is very difficult to probe the various factors—membrane rigidity and the presence of the parasite, for instance—separately. Antia et al. (7) concluded that “most studies that measure changes in RBC deformability are unable to distinguish between the underlying structural factors that contribute to these changes.”

This article reports an attempt to use numerical simulations to quantify the relative importance of the membrane elasticity and the merozoites in iRBCs. In a smoothed-particle-hydrodynamics framework, we represent the elastic membrane, cytosol, and merozoites by discrete particles. Then we simulate the stretching of RBCs by optical tweezers (8) over a range of  $G_s$  values and merozoite sizes. The other two parameters, cell shape and cytoplasmic viscosity, will be chosen from measured data and remain fixed. The main finding is that the presence of a sizeable merozoite greatly reduces the ability of the iRBC to deform under stretching. This confirms the supposition of Nash et al. (5). A prescribed amount of loss of deformability can be realized by different combinations of membrane modulus and merozoite size. Neglecting the merozoite contribution will lead to gross overestimation of the membrane modulus. In this sense, the conventional way of interpreting cell-stretching data is flawed.

## PHYSICAL MODEL AND NUMERICAL SCHEME

In this work, we adopt a three-dimensional particle-based model for the RBC, which is a generalization of our previous two-dimensional smoothed particle hydrodynamics (SPH) model (9). The RBC is represented by an elastic membrane enclosing a Newtonian viscous cytosol

Submitted March 1, 2012, and accepted for publication May 15, 2012.

\*Correspondence: jfeng@chbe.ubc.ca

Editor: Douglas Robinson.

© 2012 by the Biophysical Society  
0006-3495/12/07/0001/10 \$2.00

doi: 10.1016/j.bpj.2012.05.026

and possibly merozoites. Each component is discretized by particles. The membrane consists of a more or less uniformly distributed set of particles connected by elastic springs (Fig. 1). The cytosol is discretized by standard SPH particles that flow according to the Navier-Stokes equations. The merozoite is a stiff object, and is realized numerically by constraining a set of SPH particles to move as a rigid body (10). Thus, the membrane and merozoite particles not only play their conventional role in SPH as interpolating points, but also carry new physics that define membrane elasticity and merozoite rigidity. When simulating the stretching experiments (1,8), we ignore the viscous flow of the ambient fluid because it plays no role in the final stretching. A constant ambient pressure is applied on the RBC membrane. Overall, our model is similar in spirit to those of Tsubota et al. (11), Imai et al. (12), Pivkin and Karniadakis (13), and Fedosov et al. (14). But there are several differences in the treatment of the elasticity of the membrane, as will be explained shortly.

### Elasticity of the RBC membrane

In our physical model, the RBC membrane includes the bilipid layer as well as the underlying spectrin network. Therefore, a general viscoelastic model should be used (15). Because we are only interested in the steady-state stretching under a fixed load, we have neglected membrane viscosity and treated the membrane as purely elastic, with an in-plane shear modulus and a bending modulus.

We start with an analytical formula for the surface of a biconcave healthy red blood cell (16),

$$z = \pm \frac{R_0}{2} \left[ 1 - \frac{x^2 + y^2}{R_0^2} \right]^{1/2} \left[ c_0 + c_1 \frac{x^2 + y^2}{R_0^2} + c_2 \left( \frac{x^2 + y^2}{R_0^2} \right)^2 \right], \quad (1)$$

where  $R_0 = 3.91 \mu\text{m}$  is the cell radius on the central plane,  $c_0 = 0.207161$ ,  $c_1 = 2.002558$ , and  $c_2 = -1.122762$ . Similar to prior network models (e.g., Fedosov et al. (3), Imai et al. (12), and Boey et al. (17)), this surface is discretized into roughly equilateral triangles, with a prescribed mesh size matching the particle spacing in the bulk fluid. We deploy SPH particles on the vertices of the triangles, and connect each pair of neighbors by a linear spring,

$$\mathbf{f}_{ij} = k(r_{ij} - r_{0,ij}) \frac{\mathbf{r}_{ij}}{r_{ij}}, \quad (2)$$

where  $k$  is the spring constant, and  $r_{ij} = |\mathbf{r}_j - \mathbf{r}_i|$  is the length of the spring connecting particles  $i$  and  $j$ , with a resting length  $r_{0,ij}$  equal to its natural length on the undeformed RBC surface. Note that the same  $k$  is assigned to all springs, though their  $r_{0,ij}$  may differ slightly. As our spring network comprises largely uniform equilateral triangles, we take its overall shear and Young's modulus to be

$$G_s = \frac{\sqrt{3}}{4}k \quad \text{and} \quad E = \frac{2}{\sqrt{3}}k.$$

For bending elasticity, we adopt the spontaneous curvature model of Helfrich, with a surface force density (18),

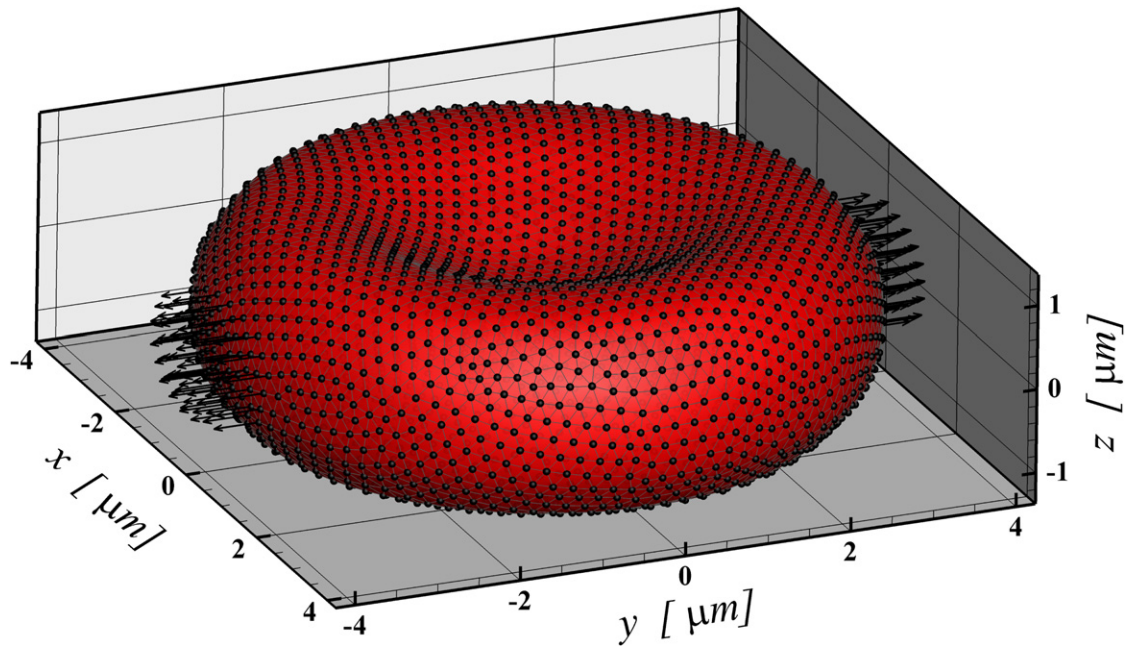


FIGURE 1 Discretization of a healthy RBC by SPH particles. The membrane is represented by elastic springs connecting neighboring particles into a more or less uniform network. The total number of particles in this case is 13,540. The arrows represent the stretching force applied by optical tweezers.

$$\boldsymbol{\tau}_b = -k_b[(2H - C_0)(2H^2 - 2K + C_0H) + 2\nabla_s^2 H]\mathbf{n}, \quad (3)$$

where  $k_b$  is the bending modulus,  $H$  and  $K$  are the local mean curvature and Gaussian curvature,  $C_0$  is the spontaneous curvature, and  $\mathbf{n}$  is the normal vector.  $\nabla_s^2$  is the surface Laplacian. When the RBC is stretched, the surface triangles are stretched as well, and the accuracy in computing the curvatures and the surface Laplacian tends to decline. This puts a limit on the amount of stretching that can be computed with confidence; the results to be presented are for stretching forces up to 150 pN.

It is interesting to note the connections and differences between our model and previous ones. For in-plane elasticity, the spectrin network models (13,15,17) use the nonlinear wormlike chain model, which is more sophisticated than our linear spring. The SPH model of Imai et al. (12) has linear springs connecting particles, whereas that of Hosseini and Feng (9) adopts nonlinear springs that approximate the area-conserving Skalak model (19). A common feature of all these and our model is that the undeformed biconcave shape is chosen as the reference state in which the in-plane elasticity is entirely relaxed. Note, however, the prestress model of Boey et al. (17). The bending elasticity is often expressed in terms of the angle  $\theta$  between neighboring triangles (12,15,20). But  $\theta$  depends on the surface tessellation and would become smaller with finer discretization. Thus, when the network is coarsened or refined, one must adjust the spontaneous angle between neighbors (13,15) and even the associated elastic constant (12). Ultimately, the stretching of RBCs is dominated by in-plane elasticity, and bending has little effect (20).

Finally, several previous models have incorporated additional energies to penalize variation in the surface area and the volume of the RBC (12,15,17). In our model, incompressibility of the cytosol ensures conservation of the cell volume, but total area conservation is not strictly enforced. For the parameters we have used here, the maximum area increase is 12% for the largest stretching forces, which is much higher than the 2–3% area expansion that can be tolerated by RBC in reality (21). To improve area conservation, one approach is to employ an additional term in the membrane elasticity to penalize local area change (15), and another is to use nonlinear springs that is stiff against area dilatation (e.g., Hosseini and Feng (9)). These are being pursued in ongoing work.

## Numerical method

Being meshless, SPH deals well with complex fluid-solid interactions with large interfacial deformation (22). Because the problem under examination in this article involves the slow stretching of RBCs with vanishing Reynolds number, we use the weakly compressible scheme for its simplicity,

with density variation controlled to within 1%. Generalities of the method can be found in previous reviews (e.g., Monaghan (10)). In a Lagrangian framework, the governing equations are

$$\frac{D\rho}{dt} = -\rho\nabla\cdot\mathbf{v}, \quad (4)$$

$$\frac{D\mathbf{v}}{Dt} = \frac{1}{\rho}\nabla\cdot\boldsymbol{\tau} - \frac{1}{\rho}\nabla p + \mathbf{f}_m, \quad (5)$$

$$\frac{p}{p_0} = \left(\frac{\rho}{\rho_0}\right)^7 - 1, \quad (6)$$

where  $D/Dt$  is the material derivative,  $\boldsymbol{\tau}$  is the viscous stress tensor, and  $\mathbf{f}_m$  is the membrane force per unit mass, which is the sum of shearing and bending forces for membrane particles and is zero for fluid particles. The symbols  $\rho_0$  and  $p_0$  are reference density and pressure, respectively, chosen to ensure a sufficiently high speed of sound. To solve these equations, we deploy a large number of particles in the domain, each carrying the dynamic properties of the field and moving in a Lagrangian framework according to ordinary differential equations that result from discretizing these partial differential equations. Particles representing the parasite are constrained to move as a rigid body according to the total hydrodynamic force on them. These special particles do not follow Eq. 5.

We advance explicitly in time by a two-step prediction-correction algorithm (9). Our three-dimensional hydrodynamic solver is based on the open-source software SPPhysics, ver. 2.2 (23), and we have added the treatment of the cell membrane and floating merozoites inside the iRBC. To determine the required spatial resolution for accurate results, we have run a series of stretching simulations with increasing numbers of particles. Fig. 2 plots the steady-state elongation of the RBC as a function of the total number of particles. Somewhat surprisingly, even a very coarse resolution with 361 particles captures the final deformation within 7%. This may be because the final deformation does not depend on the dynamics of the flow and is thus an easy quantity to compute. All results to be presented below have been computed using 13,540 particles, with 2930 on the membrane. This corresponds to an interparticle separation of  $0.051 R_0$ .

## RESULTS AND ANALYSIS

Stretching cells by optical tweezers is a popular method for probing their deformability and extracting their elastic properties (1,8). The measured deformation may be fitted to computations to yield an effective membrane modulus. In the experiments, the stretching force is applied through silica beads attached to opposite ends of the RBC. In our

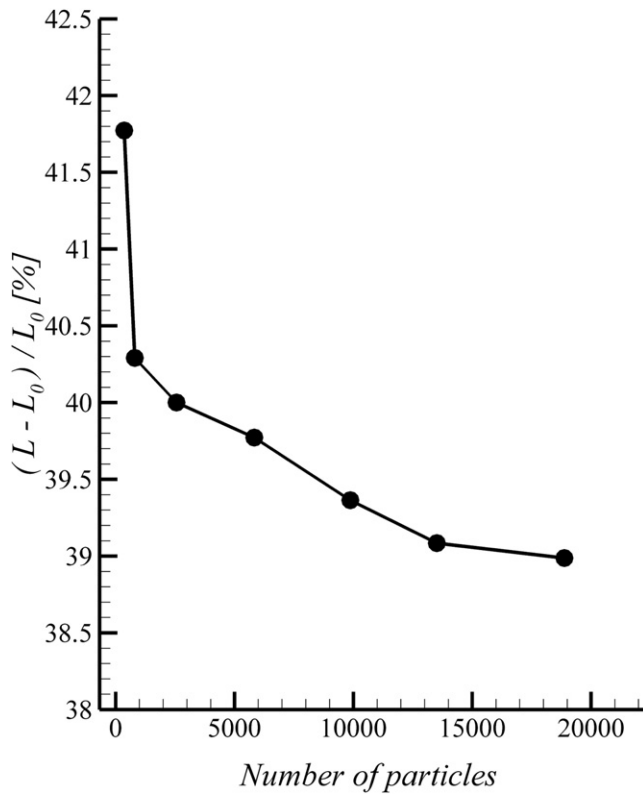


FIGURE 2 Convergence test: steady stretching of the length ( $L$ ) of a model RBC, relative to the undeformed length  $L_0 = 2R_0$ , as a function of the total number of SPH particles. The RBC contains no merozoites inside, and has a membrane shear modulus  $G_s = 15 \mu\text{N/m}$  and a bending modulus  $k_b = 6 \times 10^{-19} \text{ J}$ . The stretching force  $F = 100 \text{ pN}$ .

simulations, we mark 2% of the membrane particles on each end as “contact particles” (13,15), and apply the total force evenly divided among them (see Fig. 1). The cell deformation is simulated until a steady state is achieved. For iRBCs in each stage of infection, we choose an undeformed shape for the cell based on observations, and systematically examine how the membrane shear modulus  $G_s$  and merozoite size influence the deformability of the iRBC. For all simulations, we fix the bending modulus at  $k_b = 6 \times 10^{-19} \text{ J}$ , and the cytosol density and viscosity at  $1050 \text{ kg/m}^3$  and  $4.1 \text{ mPa}\cdot\text{s}$ , respectively. These are based on measurements of healthy RBCs (e.g., Evans and Skalak (24) and Sleep et al. (25)). Little data are available for iRBCs, but these three parameters are unimportant to the steady-state stretching.

### Stretching of healthy RBC

As a baseline, we have first computed the stretching of a healthy RBC from the equilibrium shape given by Eq. 1. Engelhardt and Sachmann (4) measured a membrane shear modulus of  $G_s = 6.1 \mu\text{N/m}$  for healthy RBC, and Nash et al. (5) reported values between 4 and  $8 \mu\text{N/m}$ . Therefore it seems reasonable to take  $G_s = 6 \mu\text{N/m}$ . The steady-state

longitudinal and transverse dimensions of the stretched cell, as functions of the stretching force, are plotted in Fig. 3. Experimental data and two prior computations are also shown for comparison. Our numerical prediction of the cell length  $L$  agrees closely with experimental data. But the narrowing of the width  $W$  is considerably underpredicted. This discrepancy may be due to simplifications in our physical model and the parameter values. For example, the elastic springs are assumed linear, and there is no rigid constraint on area conservation. In our computation, the area increases by 12% for the largest stretching force  $F = 100 \text{ pN}$ . Healthy RBCs exhibit considerable variations in  $G_s$ , and our computation has used the mean value.

Moreover, it is interesting to compare our simulation with those of Imai et al. (12) and Fedosov et al. (3). The model of Imai et al. differs from ours in the bending elasticity and the inclusion of a total area conservation term. Their shear and bending moduli have been chosen by fitting the experimental data. On the other hand, our  $G_s$  and  $k_b$  values are from measurements; it is notable that the two computations agree so closely. The dissipative-particle-dynamics simulation of Fedosov et al. (3) agrees better with experiment than ours, especially in the shrinkage of the cell width. Their model is more sophisticated in employing nonlinear springs and additional constraints on the conservation of

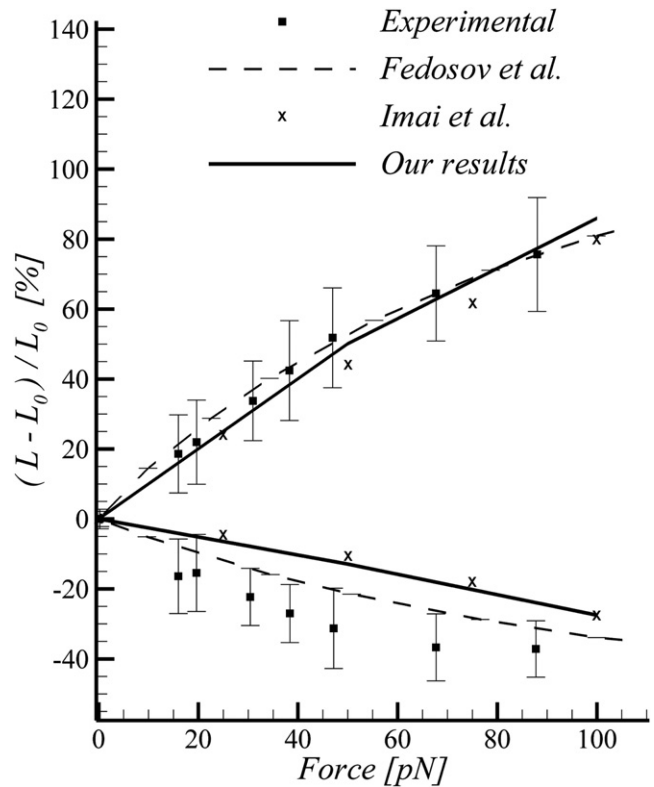


FIGURE 3 Variation of the length (upper branch) and width (lower branch) of the healthy RBC with the stretching force. The results of our numerical simulation are compared with experimental data (1) and prior computations of Imai et al. (12) and Fedosov et al. (3).

cell volume and surface area. Their effective shear modulus  $G_s = 6.3 \mu\text{N/m}$  is close to ours. Their bending modulus  $k_b = 2.4 \times 10^{-19} \text{ J}$  is much smaller but this should not have affected the deformation of the cell (20).

### Stretching of RBC in the ring stage

Upon penetrating an RBC, the malaria merozoite flattens into a thin disk. By the midring stage, it has a diameter of  $2\text{--}3 \mu\text{m}$  and a thickness of  $\sim 0.5 \mu\text{m}$  (26). Shapes and sizes of the infected RBC in the ring stage are similar to those of healthy RBCs, with a small percentage of the host volume being occupied by the parasite (27). The initial condition for the stretching simulation is the equilibrium biconcave profile of the healthy RBC (Fig. 1). Experimental data on the shear modulus  $G_s$  in the ring stage show considerable variations (5,28,29). The latest measurement (29) by membrane refractive index and nanoscale fluctuations gives  $G_s = 15.3 \mu\text{N/m}$ , and recent computations (1,3) have used similar values. We have adopted  $G_s = 15 \mu\text{N/m}$  for the simulations in this subsection.

To probe the effect of the merozoite, we first run the stretching simulation without one inside the RBC. Then we have tested two sizes of the solid disk, with a thickness of  $0.5 \mu\text{m}$  and diameters of  $2$  and  $3 \mu\text{m}$ , in several configurations: oriented in the  $xy$ ,  $yz$ , or  $zx$  planes and located near one of the ends being stretched or farthest from them (see Fig. 1). Our main finding is that with its small size, the merozoite in the ring stage has negligible effects on the deformation of the cell when stretched. Fig. 4 plots the deformation of the RBC without merozoites as solid lines, and indicates the variations due to different merozoite sizes and configurations as the error bars at  $150 \text{ pN}$ . In all situations, the effect of merozoite on the RBC deformation is  $<5\%$ . In addition, using  $G_s = 15 \mu\text{N/m}$  and the same biconcave resting shape as the healthy RBC, the numerical prediction in Fig. 4 agrees reasonably well with experimental data. Similar agreements have been noted by earlier computations using parameter values close to ours (1,3).

### Stretching of RBC in the trophozoite stage

During the trophozoite stage, the parasite is at its metabolically most active. It secretes and exports proteins onto the RBC membrane that modify its structure and permeability. As a result, the membrane's elastic modulus increases (1,30), and the shape, volume, and surface area of the cell change as well (27,31). There is a great deal of variation in the published data on the shape and size of both the iRBC and the merozoite in the trophozoite stage. Roughly speaking, the iRBC is more or less axisymmetric, but with asymmetry between the two ends of the elongated axis. In addition, there are many bumps and depressions on the surface. Meanwhile, the parasite itself increases in size

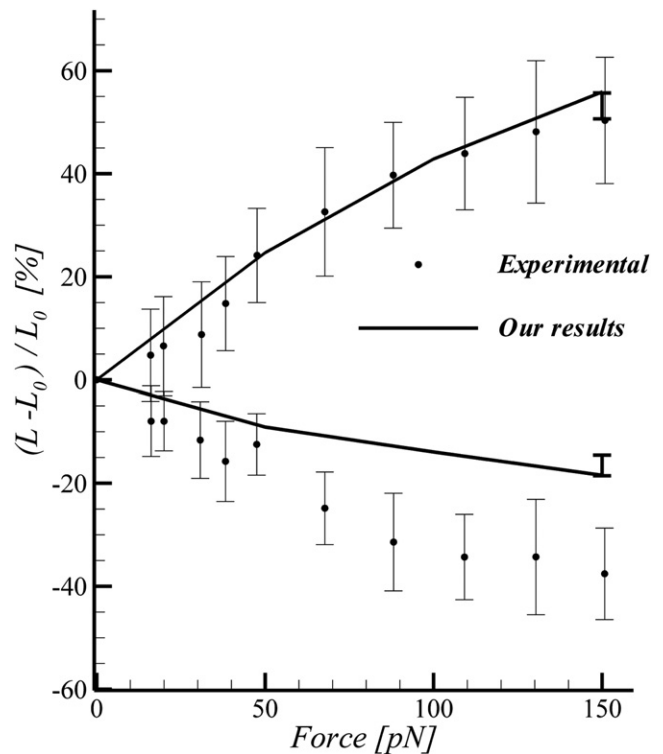


FIGURE 4 Variation of the length and width of the iRBC as a function of the stretching force in the ring stage. The solid curves are computation at  $G_s = 15 \mu\text{N/m}$  without any merozoites. The error bars on the computed result at  $150 \text{ pN}$  indicate variations due to inclusion of a disk-shaped merozoite in different sizes and configurations. The experimental data of Suresh et al. (1) are also plotted for comparison.

and becomes more spherical, eventually reaching roughly  $4 \mu\text{m}$  across (26).

Based on these observations, we have adopted an elongated axisymmetric shape for the RBC (Fig. 5). We select the dimensions of the model iRBC to match the volume

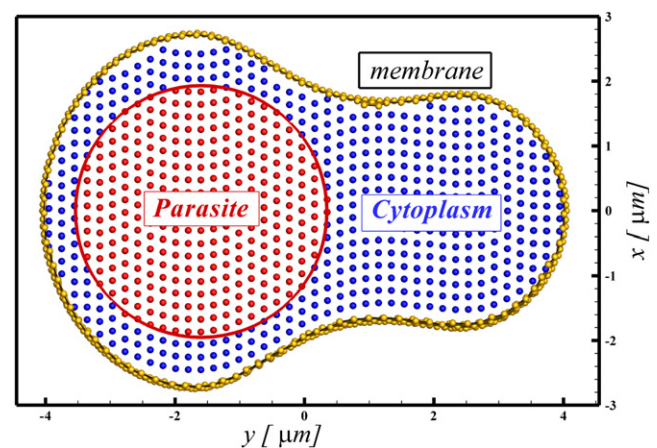


FIGURE 5 Axisymmetric model for the trophozoite-stage iRBC, with a spherical merozoite located in the thicker part of the cell, centered at  $y = -1.65 \mu\text{m}$ .

and length measured by two experiments (27,31), which are the most recent and in agreement. The surface area is  $\sim 2\%$  less than the measured value. We represent the merozoite as a rigid sphere initially located in the thicker part of the iRBC (Fig. 5). We have tested a range of merozoite sizes, with radius up to  $R_m = 2.25 \mu\text{m}$  and volume up to 47% of total iRBC volume (27). The initial center of the parasite is always  $1.65 \mu\text{m}$  below the midpoint of the iRBC. After tessellation of the RBC membrane, we again take the length of each link to be the resting length of the elastic spring (Eq. 2) such that the in-plane elasticity is fully relaxed in the undeformed shape of Fig. 5.

As a result of the aforementioned structural and conformational changes, iRBCs in the trophozoite stage become much less deformable than their healthy counterpart. Conventionally, this loss of deformability is ascribed to an elevated membrane stiffness. Several groups have used an effective shear modulus  $G_s$ , ranging from 21.3 to  $40 \mu\text{N/m}$  to explain the reduced deformation of the iRBC when stretched (1–3,12). On the other hand, micropipette aspiration of small areas of the membrane shows a much lower local modulus, 9– $18 \mu\text{N/m}$  (5,6). In the following, we explore the effect of the parasite particle on the overall deformability of iRBC with our numerical model, and demonstrate that the current practice of attributing the loss of deformability entirely to increased membrane modulus is flawed.

We have carried out a series of simulations by varying the radius of the merozoite  $R_m$  from 0 to  $2.25 \mu\text{m}$ , and separately the membrane shear modulus  $G_s$  from 10 to  $27.5 \mu\text{N/m}$ . The stretching force is fixed at  $F = 150 \text{ pN}$  in these simulations. The final axial length of the cell, after attaining steady-state stretching, is plotted in Fig. 6 a as a function of  $R_m$  and  $G_s$ . The relative deformation  $(L - L_0)/L_0$  decreases with both  $G_s$  and  $R_m$ . The dependence on  $R_m$  is relatively mild for smaller merozoites, reminiscent of the lack of an effect in the ring stage (Fig. 4). But for larger  $R_m$ , the deformability plunges precipitously, as the stretching entails

narrowing of the transverse dimension of the cell with the membrane pressing onto the rigid merozoite inside.

The most interesting observation of Fig. 6 a is a kind of compensation between  $G_s$  and  $R_m$ ; a certain amount of deformability can be reached by having a larger merozoite paired with a softer membrane, or a smaller merozoite with a stiffer membrane. To illustrate this compensation more quantitatively, we note that experiments have reported a 39% axial lengthening of iRBC when stretched by  $F = 150 \text{ pN}$  in the trophozoite stage (1). By cutting the deformation surface of Fig. 6 a by the horizontal plane of 39% deformation, we obtain the intersection curve by linear interpolation and plot it in Fig. 6 b. Clearly, the 39% overall deformation observed in the experiment could have been produced by an infinite number of  $(R_m, G_s)$  combinations. In particular, for  $R_m = 2.15 \mu\text{m}$  observed in late trophozoite stage (27), the 39% deformation requires a membrane shear modulus of  $G_s = 18.2 \mu\text{N/m}$ , comparable with the local modulus of 9– $18 \mu\text{N/m}$  measured by aspiration of small membrane tongues (5,6). On the other hand, extrapolating the curve toward  $R_m = 0$  will give  $G_s$  values of  $\sim 30 \mu\text{N/m}$ , consistent with those obtained by interpreting the loss of deformability entirely as due to an increasing  $G_s$  (3). Thus, the discrepancy in  $G_s$  in the literature is explained by the existence of the solid merozoite.

### Stretching of RBC in the schizont stage

During the schizont stage, the merozoite undergoes several rounds of mitosis that results in 16–20 daughter merozoites. These, along with a remnant body of hemozoin crystals, are tightly enclosed within a compact digestive vacuole at the center of the iRBC (26). The total volume of the parasites at the end of the schizont stage, according to various estimations, ranges from  $20 \mu\text{m}^3$  to  $63 \mu\text{m}^3$ , the upper bound amounting to 83% of the total cell volume (27). Meanwhile, the volume of the cell shrinks from the trophozoite stage, with the iRBC taking on a more rounded shape, eventually

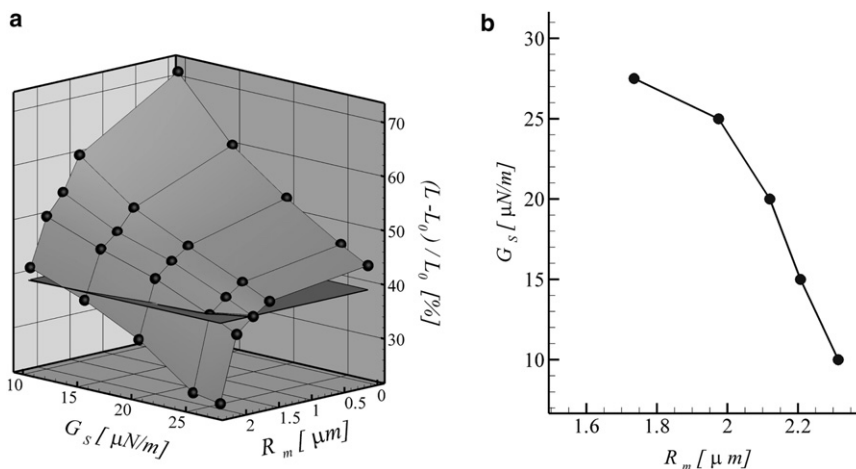


FIGURE 6 (a) Stretching of a trophozoite-stage iRBC, under a force of  $F = 150 \text{ pN}$ , as a function of the membrane shear modulus  $G_s$  and the merozoite radius  $R_m$ . The horizontal plane is at 39% elongation, the experimentally observed amount. (b) The intersection of the 39%-elongation plane and the deformation surface, plotted on the  $(G_s, R_m)$  plane.

bursting at the end of the schizont stage (26,27,31). Experiments disagree on how the iRBC surface area changes from the trophozoite to the schizont stage (5,27,31). Inspired by experimental images and prior computations (3,26), we have used an oblate spheroid to represent the iRBC in schizont stage (Fig. 7). The three axes,  $6.9 \times 6.9 \times 3.2 \mu\text{m}$ , are chosen to match closely the volume and surface area reported by Esposito et al. (31). The tightly packed parasites will be modeled as a single oblate spheroid with the same aspect ratio as the iRBC, centered inside the red cell. Its size will be varied in the simulations to demonstrate the effect of the parasites on the stretching of the iRBC. The in-plane elasticity is assumed to be relaxed for the undeformed membrane shape of Fig. 7.

Fig. 8 *a* depicts a deformation surface similar to that of Fig. 6 *a*; the percentage elongation of the iRBC is plotted as a function of the membrane shear modulus  $G_s$  and the parasite/iRBC volume ratio  $v$ . The stretching force is fixed at 100 pN. The deformation decreases with both  $G_s$  and  $v$ , as expected. In particular, the presence of the parasite plays a significant role in hampering the deformation of the iRBC as a whole, as speculated by Nash et al. (5), and the effect is stronger for smaller  $G_s$ . This is probably because a softer membrane deforms easily to hug the contour of the parasite, thus allowing its effect to be fully manifested. A stiff membrane, in contrast, holds its shape well under stretching and partially shields the effect of the solid inclusion.

To illustrate the interaction between the parasite and the membrane, we plot the profile of the membrane strain in the symmetry plane of the stretched iRBC (Fig. 9). This is generated by computing the finite Green-Lagrange strain experienced by membrane particles within  $0.0225R_0$  of the central plane,

$$\epsilon = \frac{1}{2}(\lambda^2 - 1), \quad (7)$$

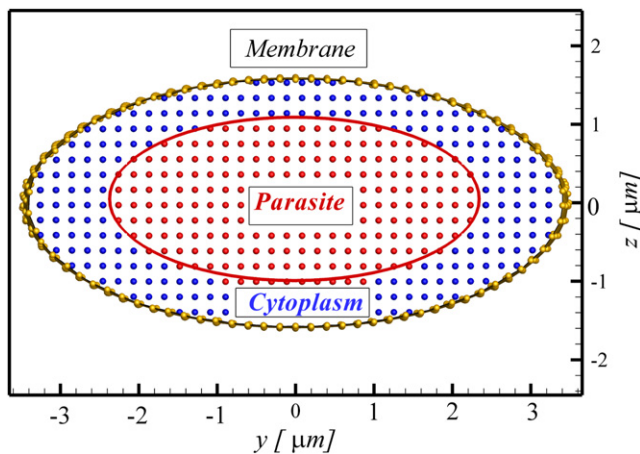


FIGURE 7 Cross section of the oblate spheroid model for the schizont-stage iRBC. The parasite is represented by an oblate spheroid of the same aspect ratio as the whole cell.

where  $\lambda$  is the principle stretch ratio, and then indicating the magnitude of  $\epsilon$  by the length of a vector along the normal direction. Without the parasite, the strain is maximum at a short distance from the ends, and decreases gradually toward the middle of the cell. The large parasite, occupying 60% of the total volume, forces the membrane to conform to its contour when stretched. This reduces the local strain by roughly 50%. Relative to the undeformed iRBC diameter of  $6.9 \mu\text{m}$ , the amount of stretching decreases from 41.4% without the parasite, to 34.6% with it. The mechanical effect of the solid parasites in reducing the deformability of the cell is thus unequivocally established.

The experiment of Suresh et al. (1) reported 22% elongation of the iRBC in the schizont stage under a stretching force of  $F = 100 \text{ pN}$ . Intersecting the deformation surface by a horizontal plane at 22%, we obtain the curve of Fig. 8 *b* that plots the  $G_s$  and  $v$  combinations that would produce the observed amount of deformation. Again, we note a compensation effect between the two factors; a larger parasite may compensate for a softer membrane, and vice versa. Three points are particularly interesting: 1), For the actual parasite volume ratio  $v \approx 80\%$  in the late schizont stage (27), the 22% deformation requires a membrane shear modulus of  $G_s \approx 16.8 \mu\text{N/m}$ . This is reasonably close to the range (9–14  $\mu\text{N/m}$ ) estimated from micropipette aspiration (5). 2), The estimation of  $G_s \approx 16.8 \mu\text{N/m}$  is also close to the value of 18.2  $\mu\text{N/m}$  obtained from Fig. 6 *b* in the trophozoite stage. This suggests that the membrane modulus stays relatively unchanged in the later stages of infection. This is plausible in view of observations (5), but we have found no definite data to confirm it. 3), Given the significant contribution of the parasite to the loss of iRBC deformability, neglecting it would lead to an overestimation of the membrane modulus. Fig. 8 *b* would suggest  $G_s = 35 \mu\text{N/m}$  in the absence of the parasite, an overestimation by a factor of 3–4 above the locally measured values. This is comparable to  $G_s = 40 \mu\text{N/m}$  used by Fedosov et al. (3) to produce the proper amount of deformation without including the parasite, and further below those used in earlier calculations (1,2) ranging between 50 and 60  $\mu\text{N/m}$ .

The simulations for the three erythrocytic stages of malaria infection have used different RBC shapes and parasite configurations. By correlating the progressive loss of deformability with the various parameters, we can identify the separate contributions of membrane stiffness, RBC shape, and parasite size. Table 1 lists data extracted from the simulations at parameters representative of measured values in each stage (e.g., Serebrennikova et al. (27) and Esposito et al. (31)). Note that: 1), The difference in  $\lambda_0$  between the ring and the healthy states is mostly due to the elevated  $G_s$ ; this amounts to a loss of almost half of the deformability. 2), Comparing  $\lambda_0$  among the three infected stages gives us the contribution of the cell shape or  $S/V$  to the total loss of deformability in terms of  $\lambda_p$ . The

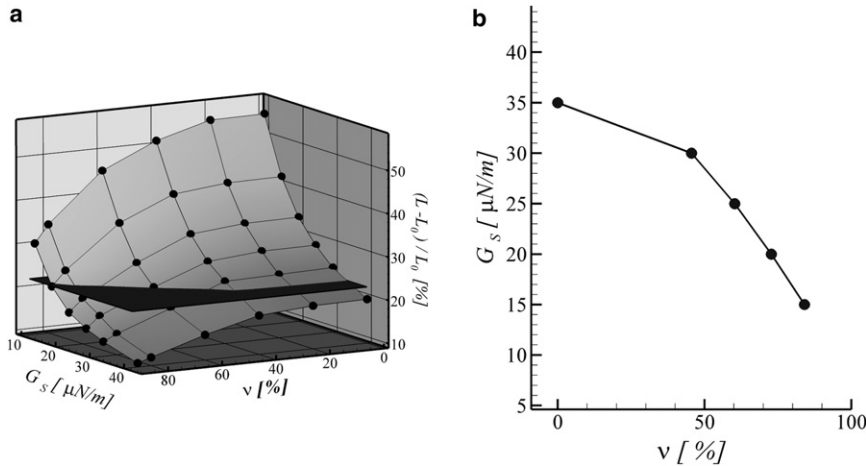


FIGURE 8 (a) Stretching of a schizont-stage iRBC, under a force of  $F = 100$  pN, as a function of the membrane shear modulus  $G_s$  and the parasite/iRBC volume ratio  $v$ . The horizontal plane is at 22% deformation, the experimentally observed amount. (b) The intersection of the 22%-deformation plane and the deformation surface, plotted on the  $(G_s, v)$  plane.

difference  $\lambda_p - \lambda_o$  for each stage then gives the contribution due to the parasite. Using  $\lambda_o = 43.9\%$  in the ring stage as the baseline, the trophozoite deformability decreases to  $\lambda_p = 31.2\%$ . Of this decrease of 12.7 percentage points,  $S/V$  contributes  $(43.9 - 38.9)/12.7 = 39.4\%$  and the parasite contributes the rest (60.6%). For the schizont, these two contributions are 13.0% and 87.0%, respectively. In this case, the dominance of the parasite contribution is because of the relatively small reduction in  $S/V$  from the ring to the schizont stage. In reality, various attributes of the iRBC change simultaneously. It is thanks to the power of numerical computations that one may extract a quantitative measure of the effect of the individual factors.

## SUMMARY

This study is based on a simple mechanical argument that the presence of a solid parasite inside the red cell should affect its overall deformation. If the solid is of a substantial size, it will conceivably interfere with the deformation of the membrane when the cell is stretched. This was hypothesized by Nash et al. (5) more than 20 years ago, but overlooked in subsequent experimental and computational studies on stretching RBCs by optical tweezers. Using a relatively simple particle-based model, we have carried out detailed computations that have quantified the mechanical effect of solid parasites in hampering overall cell deformation.

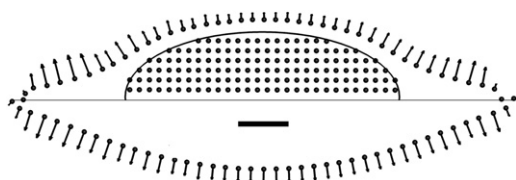


FIGURE 9 Symmetry plane of the stretched iRBC with a parasite having 60% of the total volume in the schizont stage (top), compared with that without the parasite (bottom).  $F = 100$  pN and  $G_s = 15$   $\mu\text{N/m}$  in both cases. The length of the vectors indicates the local principal strain  $\epsilon$ , the horizontal scale bar corresponding to  $\epsilon = 1$ .

In the ring stage, we show that the parasite volume is too small to have much effect on the cell deformation. In this case, the previous assumption that the increased RBC rigidity is entirely due to elevated membrane modulus is correct. In the trophozoite and schizont stages, on the other hand, the red cell membrane tends to press against the solid parasite when sufficiently stretched. This leads to a significant reduction in the cell deformability. In each case, we show that the measured size of the parasite coupled with the locally measured membrane shear modulus will produce the correct amount of iRBC rigidification. Ignoring the parasite and attributing the loss of deformation solely to the membrane rigidity would overestimate the membrane modulus by more than a factor of 2 in the trophozoite stage and up to a factor of 4 in the schizont stage. This explains the discrepancy between the membrane shear modulus locally measured by micropipette aspiration and that globally estimated from whole-cell stretching. From the numerical data, we have identified the individual contributions of cell shape, membrane modulus, and parasite to the overall loss of deformability.

We must point out the assumptions and limitations of the model that may have affected the fidelity and accuracy of the results. The actual RBC membrane has a complex structure, and only the grossest features are retained in our

TABLE 1 Comparison of RBC stretching under  $F = 100$  pN for geometric and physical parameters typical of the healthy cell and the three stages of malaria infection

	$G_s$ ( $\mu\text{N/m}$ )	$S/V$ ( $\mu\text{m}^{-1}$ )	$v$ (%)	$\lambda_p$ (%)	$\lambda_o$ (%)
Healthy	6	1.42	0	—	86.0
Ring	15	1.42	3.80	41.6	43.9
Trophozoite	15	1.14	40.5	31.2	38.9
Schizont	15	1.25	80.0	24.7	41.4

$S/V$  is the area-volume ratio of the undeformed cell. The expression  $\lambda_p = (L - L_0)/L_0$  is the relative stretching of the iRBC containing a parasite of the indicated volume. The value  $\lambda_o$  is the stretching of the same iRBC membrane, but with the parasite removed.

particle-linear-spring network. The most severe shortcoming is the lack of area conservation. The linearity of the spring leads to only a moderate amount of strain-hardening at large deformation. One way to address this issue is to use nonlinear springs designed to be strongly resistant to areal dilatation or compression (9), in the spirit of the continuum Skalak model (19). In addition, we have neglected the viscosity of the membrane partly because this work focuses on the steady-state stretching instead of the dynamic transient. The membrane should be treated as viscoelastic in dynamic situations. Similarly, we have disregarded the liquid medium surrounding the cell, which should be included if the transient of the cell deformation is of interest.

We have focused on the steady-state cell stretching by optical tweezers. The same methodology can be used to study effects of the parasite on the dynamics of infected red cells (3,14,32). More generally, it may be useful to the exploration of the fundamental question of cell response to forcing. Examples include the transit of various blood cells in microfluidic devices designed for cell sorting or cytometric analysis, and the mechanical activation of neutrophils in microcapillaries. In a recent review, Hoffman and Crocker (33) noted the difficulty in understanding how external force propagates through different intracellular structures, and called for the development of “a detailed model for the (dynamic) mechanical response of all the relevant load-bearing structures in the cell and their interconnections.” Our particle-based model for *P. falciparum*-infected RBC is a modest effort toward that goal.

We thank Dmitry Fedosov (Forschungszentrum Jülich), Giovanni Ghigliotti (University of British Columbia), George Karniadakis (Brown University), Chwee-Teck Lim (National University of Singapore), and Tenghu Wu (University of British Columbia) for helpful discussions.

We acknowledge support by the Petroleum Research Fund, the Canada Research Chair program, Natural Sciences and Engineering Research Council (Discovery and Strategic grants and Accelerator Supplement), and the Canada Foundation for Innovation.

## REFERENCES

- Suresh, S., J. Spatz, ..., T. Seufferlein. 2005. Connections between single-cell biomechanics and human disease states: gastrointestinal cancer and malaria. *Acta Biomater.* 1:15–30.
- Suresh, S. 2006. Mechanical response of human red blood cells in health and disease: some structure-property-function relationships. *J. Mater. Res.* 21:1871–1877.
- Fedosov, D. A., B. Caswell, ..., G. E. Karniadakis. 2011. Quantifying the biophysical characteristics of *Plasmodium-falciparum*-parasitized red blood cells in microcirculation. *Proc. Natl. Acad. Sci. USA.* 108:35–39.
- Engelhardt, H., and E. Sackmann. 1988. On the measurement of shear elastic moduli and viscosities of erythrocyte plasma membranes by transient deformation in high frequency electric fields. *Biophys. J.* 54:495–508.
- Nash, G. B., E. O'Brien, ..., J. A. Dormandy. 1989. Abnormalities in the mechanical properties of red blood cells caused by *Plasmodium falciparum*. *Blood.* 74:855–861.
- Glenister, F. K., R. L. Coppel, ..., B. M. Cooke. 2002. Contribution of parasite proteins to altered mechanical properties of malaria-infected red blood cells. *Blood.* 99:1060–1063.
- Antia, M., T. Herricks, and P. K. Rathod. 2008. Microfluidic approaches to malaria pathogenesis. *Cell. Microbiol.* 10:1968–1974.
- Dao, M., C. T. Lim, and S. Suresh. 2003. Mechanics of the human red blood cell deformed by optical tweezers. *J. Mech. Phys. Solids.* 51:2259–2280.
- Hosseini, S. M., and J. J. Feng. 2009. A particle-based model for the transport of erythrocytes in capillaries. *Chem. Eng. Sci.* 64:4488–4497.
- Monaghan, J. J. 2005. Smoothed particle hydrodynamics. *Rep. Prog. Phys.* 68:1703–1759.
- Tsubota, K., S. Wada, and T. Yamaguchi. 2006. Particle method for computer simulation of red blood cell motion in blood flow. *Comput. Methods Programs Biomed.* 83:139–146.
- Imai, Y., H. Kondo, ..., T. Yamaguchi. 2010. Modeling of hemodynamics arising from malaria infection. *J. Biomech.* 43:1386–1393.
- Pivkin, I. V., and G. E. Karniadakis. 2008. Accurate coarse-grained modeling of red blood cells. *Phys. Rev. Lett.* 101:118105.
- Fedosov, D. A., B. Caswell, and G. E. Karniadakis. 2011. Wall shear stress-based model for adhesive dynamics of red blood cells in malaria. *Biophys. J.* 100:2084–2093.
- Fedosov, D. A., B. Caswell, and G. E. Karniadakis. 2010. A multiscale red blood cell model with accurate mechanics, rheology, and dynamics. *Biophys. J.* 98:2215–2225.
- Evans, E., and Y. C. Fung. 1972. Improved measurements of the erythrocyte geometry. *Microvasc. Res.* 4:335–347.
- Boey, S. K., D. H. Boal, and D. E. Discher. 1998. Simulations of the erythrocyte cytoskeleton at large deformation. I. Microscopic models. *Biophys. J.* 75:1573–1583.
- Vlahovska, P. M., T. Podgorski, and C. Misbah. 2009. Vesicles and red blood cells in flow: from individual dynamics to rheology. *Comput. Methods Appl. Mech. Eng.* 10:775–789.
- Skalak, R., A. Tozeren, ..., S. Chien. 1973. Strain energy function of red blood cell membranes. *Biophys. J.* 13:245–264.
- Li, J., M. Dao, ..., S. Suresh. 2005. Spectrin-level modeling of the cytoskeleton and optical tweezers stretching of the erythrocyte. *Biophys. J.* 88:3707–3719.
- Mohandas, N., and E. Evans. 1994. Mechanical properties of the red cell membrane in relation to molecular structure and genetic defects. *Annu. Rev. Biophys. Biomol. Struct.* 23:787–818.
- Hosseini, S. M., and N. Amanifard. 2007. Presenting a modified SPH algorithm for numerical studies of fluid-structure interaction problems. *Int. J. Eng. Trans. B.* 20:167–178.
- Dalrymple, R. A., M. Gómez-Gesteira, ..., M. Narayanaswamy. 2010. Smoothed particle hydrodynamics for water waves. In *Advances in Numerical Simulation of Nonlinear Water Waves, Chapter 13*. Q. Ma, editor. World Scientific, Singapore. 465–495.
- Evans, E., and R. Skalak. 1980. *Mechanics and Thermodynamics of Biomembranes*. CRC Press, Boca Raton, FL.
- Sleep, J., D. Wilson, ..., W. Gratzer. 1999. Elasticity of the red cell membrane and its relation to hemolytic disorders: an optical tweezers study. *Biophys. J.* 77:3085–3095.
- Hanssen, E., P. J. McMillan, and L. Tilley. 2010. Cellular architecture of *Plasmodium falciparum*-infected erythrocytes. *Int. J. Parasitol.* 40:1127–1135.
- Serebrennikova, Y. M., J. Patel, ..., L. H. García-Rubio. 2010. Quantitative analysis of morphological alterations in *Plasmodium falciparum* infected red blood cells through theoretical interpretation of spectral measurements. *J. Theor. Biol.* 265:493–500.

28. Suwanarusk, R., B. M. Cooke, ..., R. Udomsangpetch. 2004. The deformability of red blood cells parasitized by *Plasmodium falciparum* and *P. vivax*. *J. Infect. Dis.* 189:190–194.
29. Park, Y., M. Diez-Silva, ..., S. Suresh. 2008. Refractive index maps and membrane dynamics of human red blood cells parasitized by *Plasmodium falciparum*. *Proc. Natl. Acad. Sci. USA.* 105:13730–13735.
30. Maier, A. G., B. M. Cooke, ..., L. Tilley. 2009. Malaria parasite proteins that remodel the host erythrocyte. *Nat. Rev. Microbiol.* 7:341–354.
31. Esposito, A., J. B. Choimet, ..., T. Tiffert. 2010. Quantitative imaging of human red blood cells infected with *Plasmodium falciparum*. *Biophys. J.* 99:953–960.
32. Veerapaneni, S. K., Y.-N. Young, ..., J. Bławdziewicz. 2011. Dynamics of a compound vesicle in shear flow. *Phys. Rev. Lett.* 106:158103.
33. Hoffman, B. D., and J. C. Crocker. 2009. Cell mechanics: dissecting the physical responses of cells to force. *Annu. Rev. Biomed. Eng.* 11:259–288.